Experiments in Fluids 33 (2002) 838–853
DOI 10.1007/s00348-002-0521-9

Particle image velocimetry measurements of a backward-facing step flow

J. Kostas, J. Soria, M.S. Chong

Abstract Particle image velocimetry (PIV) measurements were carried out on a backward-facing step flow at a Reynolds number of $Re_h=U_\infty h/\nu$=4,660 (based on step height and freestream velocity). In-plane velocity, out-of-plane vorticity, Reynolds stress and turbulent kinetic energy production measurements in the x–y and x–z planes of the flow are presented. Proper orthogonal decomposition was performed on both the fluctuating velocity and vorticity fields of the x–y plane PIV data using the method of snapshots. Low-order representations of the instantaneous velocity fields were reconstructed using the velocity modes. These reconstructions provided insight into the contribution that the various length scales make to the spatial distribution of mean and turbulent flow quantities such as Reynolds stress and turbulent kinetic energy production. Large scales are found to contribute to the Reynolds stresses and turbulent kinetic energy production downstream of reattachment, while small scales contribute to the intense Reynolds stresses in the vicinity of reattachment.

List of symbols

$a^{(k)}{}_n$	time-dependent coefficients for the kth eigenfunction
A	universal boundary layer constant
C_{mn}	spatial correlation matrix, $\frac{1}{M}\int_D f(\mathbf{x},t_m)f(\mathbf{x},t_n)\mathrm{d}\mathbf{x}$
E	energy
f	generic function
h	step height
K	upper limit index POD mode index
L	length scale
M	number of frames, snapshots, velocity realisations
N	number of spatial points in the domain
P_{ke}	turbulent kinetic energy production, $-\overline{u'_i u'_j}\frac{\partial U_i}{\partial x_j}$
Re_h	Reynolds number based on step height, $U_\infty h/\nu$
Re_δ	Reynolds number based on boundary layer thickness, $U_\infty\delta/\nu$
Re_{δ^*}	Reynolds number based on boundary layer displacement thickness, $U_\infty\delta^*/\nu$
Re_θ	Reynolds number based on momentum thickness, $U_\infty\theta/\nu$
$R(\mathbf{x},\mathbf{x}')$	two point averaged spatial correlation function
$R_{\omega_y}(x;z,z')$	spanwise auto-correlation function of mean ω_y, in the x–z plane
St	dimensionless, reduced frequency, fh/U_∞
t	time
T	time interval
u, v, w	instantaneous velocity components in x, y, z directions
$\bar{u}$, $\bar{v}$, $\bar{w}$	mean velocity components in x, y, z directions
u', v', w'	instantaneous, fluctuating velocity components in x, y, z directions
U, V, W	mean velocity components in x, y, z directions
$\mathbf{u}$	instantaneous velocity in vector notation
$\mathbf{u}'$	fluctuating velocity in vector notation
$\bar{\mathbf{u}}$	mean velocity in vector notation
u_τ	wall shear velocity
$\overline{u'_i u'_j}$	Reynolds stresses
x, y, z	rectangular Cartesian coordinates
$\mathbf{x}$	position vector in vector notation
X_{R}	mean reattachment length
y_1, y_2	upstream and downstream channel heights respectively
δ	boundary layer thickness; uncertainty
δ^*	boundary layer displacement thickness, $\int_0^\infty\left(1-\frac{u}{U_\infty}\right)\mathrm{d}y$
δ_{kl}	Kronecker delta
δ_{ω_z}	local shear layer thickness, $(U_{\max}-U_{\min})\Big/\left(\frac{\mathrm{d}U}{\mathrm{d}y}\right)_{max}$
Δ	spatial sampling separation of measurements
$\Delta\mathbf{X}$	in-plane particle displacement in vector notation
ϵ	fractional uncertainty/error
θ	boundary layer momentum thickness, $\int_0^\infty\frac{u}{U_\infty}\left(1-\frac{u}{U_\infty}\right)\mathrm{d}y$
κ	universal boundary layer constant
λ	non-dimensional random vorticity error transmission ratio, $\varepsilon_{\omega_{\mathrm{rand}}}=\lambda\varepsilon_u$
λ_k	kth eigenvalue

Accepted: 4 June 2002
Published online: 19 October 2002

J. Kostas, J. Soria (✉)
Laboratory for Turbulence Research in Aerospace and Combustion,
Department of Mechanical Engineering,
Monash University, PO Box 31, Melbourne,
Victoria 3800, Australia
E-mail: Julio.Soria@eng.monash.edu.au

M.S. Chong
Department of Mechanical and Manufacturing Engineering,
University of Melbourne, Parkville,
Victoria 3052, Australia

λ^+	non-dimensional spanwise streak spacing
ρ	fluid density
$\Phi^{(k)}{}_n$	kth eigenfunction of the spatial correlation matrix, C_{mn}
$\psi^{(k)}$	kth eigenfunction of $R(\mathbf{x},\mathbf{x}')$
ω	instantaneous, out-of-plane vorticity
ω'	non-dimensional, instantaneous, out-of-plane vorticity, $\omega h/U_\infty$
$\bar{\omega}$	mean, out-of-plane vorticity
$\boldsymbol{\omega}$	instantaneous vorticity in vector notation

Subscripts

BFS	backward-facing step
bias	bias component
fluc	fluctuating value
I, II	corresponding to regions I and II respectively
i, j	spatial coordinate indices
k	mode order index
ke	kinetic energy
max	maximum value
mean	mean value
min	minimum value
n	time index
rand	random component
rms	root mean square value
sep	value at separation
tot	total value
x, y, z	components in the x, y, z directions respectively
∞	freestream value

Superscripts

2D	two-dimensional value
+	sublayer scaled value
*	non-dimensional value; complex conjugate
′	non-dimensional value; fluctuating value

1 Introduction

Flow separation often occurs at locations of sudden changes in the surface geometry. A separated shear layer usually develops at the surface discontinuity and reattaches some distance downstream, if the surface geometry permits, forming a recirculation bubble.

A widely known separated flow geometry is the backward-facing step (BFS) flow (see Fig. 1). This geometry is of particular interest because it facilitates the study of the reattachment process by minimising the effect of the separation process, while for other separating and reattaching flow geometries there may be a strong interaction between the two.

The principal flow features of the turbulent BFS flow are described as follows: a turbulent boundary layer, of thickness δ, which forms on a flat plate, encounters a downward step of height h. The sudden expansion due to the change in surface geometry causes the boundary layer to separate at the step edge. Immediately after detachment, the flow essentially behaves as a free shear layer, with high-speed fluid on one side and low-speed fluid on the other. Some distance downstream, the shear layer impinges on the surface and forms a closed recirculation region containing turbulent, upstream moving fluid. A small "corner eddy" of the opposite rotation sense to the main recirculating flow might also exist in this region. Reattachment occurs over a region located about the time-averaged reattachment point, X_R. The flow in this zone is found to be unsteady and highly three-dimensional (3D) with large-scale structures, of size $O(h)$ passing through frequently. Downstream of reattachment, the boundary layer begins to redevelop and undergoes a relaxation to a normal turbulent boundary layer state.

The BFS flow has been studied extensively, yet much continues to be unknown about the flow structure and dynamics of this geometrically simple, turbulent flow. Vortical structures in the flow and their interactions are believed to play an important role in the generation of turbulent stresses, turbulent kinetic energy, shear layer entrainment and growth and mean flow development. However, the direct and correct identification and observation of vortical structures and their interactions in the flow has received little attention to date. Separated shear layer motions known as "flapping" and "shedding" are widely reported in the literature, but their origins are unclear. The complex dynamics of flow reattachment require further investigation, as do the boundary layer redevelopment flow dynamics. Finally, the 3D nature of the flow requires substantially more study.

Many of the investigations and the currently available data have focused on the statistical properties of the flow, obtained from single point measurement techniques such as hotwires, surface pressure sensors and laser Doppler anemometry (LDA). The physical structures in the BFS flow (and other turbulent flows for that matter) and their dynamics have been difficult to investigate with single point measurement techniques because of the difficulty involved in obtaining multi-point measurements with high

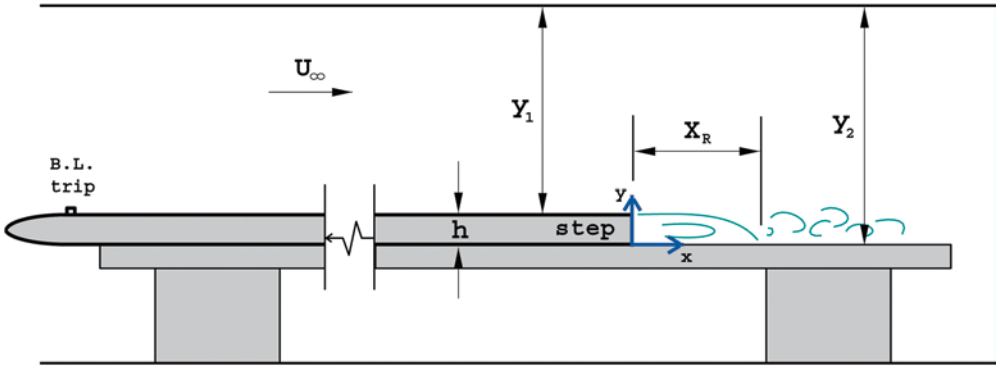

Fig. 1. Flow geometry for the BFS. The step height is h, the upstream channel height is y_1 and the downstream channel height is y_2. The mean reattachment length is represented by X_R and the freestream velocity is U_∞

spatial resolution instantaneously throughout the flow domain. Flow visualisation techniques have allowed the flow structure to be investigated, although such images can often be difficult to interpret and only give qualitative information about the flow.

The advent of multi-dimensional, quantitative measurement techniques such as particle image velocimetry (PIV) are well suited to the study of instantaneous flow structure and evolving dynamics of turbulent flows. PIV has only recently begun to gain widespread use as a tool for investigating flow dynamics and probing the structure of complex flows. This technique offers the potential to acquire instantaneous 2D measurements (with a higher spatial resolution than can be achieved with arrays of single point measurement probes) over a relatively large 2D region of the flow.

Only a few experimental investigations have obtained spatio-temporal data on the flow structure of the BFS flow, several of which will be briefly discussed here.

Grant et al. (1992) performed PIV on a BFS flow at a Reynolds number of $Re_h=U_\infty h/\nu\approx$45,000. This work compared the accuracy of their limited number of PIV samples with a large sample of velocity data acquired with an LDA probe. The number of samples required to obtain velocity statistics with PIV to a desired accuracy was considered and discussed.

Huang (1994) used a video-based PIV system to obtain spatio-temporal data on a BFS flow. The Reynolds number investigated was $Re_h\approx$4,300 and the aspect ratio of the flow was 2.5:1. It is likely that this flow was highly 3D in the mean, based on the criterion set by deBrederode and Bradshaw (1972) of at least a 10:1 aspect ratio for mean, 2D flow. Huang (1994) found problems with the reliability and accuracy of PIV measurements in regions where large velocity gradients were present in the flow. The measurement accuracy in these regions was improved over conventional PIV using a particle image distortion (PID) algorithm. Proper orthogonal decomposition was performed on the velocity and vorticity field data in an effort to identify and investigate time-dependent structures in the flow. From this analysis, Huang found that 75% of the energy resided in the first 50 modes. This was considered a relatively poor energy convergence compared with decompositions of other flows where a large proportion of the energy was captured in relatively few modes (Kirby et al. 1990; Rajaee et al. 1994; Hilberg et al. 1994; Delville et al. 1999; Gordeyev and Thomas 2000). The poor energy convergence was attributed to the large variety of scales present throughout the flow. An investigation of the time-dependent behaviour of the modes revealed two types of motion present in the recirculation region of the flow, described in their paper as a "swing" motion and an "expansion and compression" motion. POD analysis was also performed on the vorticity field and the results were compared with those obtained from the velocity decomposition. There was good agreement between the lowest-order mode of each but little similarity between the remaining corresponding modes.

A further investigation of the BFS flow using PIV was subsequently conducted by Huang and Fiedler (1997). In this case, the impulsively started flow over a step was studied. The fully developed flow had a Reynolds number of $Re_h\approx$4,300 and was found to exist for a non-dimensional time $t^*=Ut/h>40$. Five hundred images were acquired using a video-based PIV system and were analysed using the PID technique. Spectra of the velocity fluctuations in the free shear layer and at the reattachment point were calculated for the fully developed flow. A non-dimensional frequency of $St=fh/U_\infty\approx0.04$ was identified, which compares favourably with the low-frequency shedding component of the shear layer that has been observed by other investigators ($St\approx0.07$). However, the authors make a point that the sampling duration was possibly insufficient to accurately resolve this frequency.

A similar study was also performed by Brücker (1999), although the investigation was restricted solely to the transient phase of the flow. A 3D scanning PIV technique, in combination with digital high-speed video, was used to obtain the measurements. This enabled the temporal evolution of 20 planes spanning half the width of the channel to be captured. The close spacing of the planes permitted the spanwise velocity component of the flow to be calculated. Measurements were conducted at Reynolds numbers of $Re_h\approx$1,000 and $Re_h\approx$2,000, where the steady state, mean freestream velocity was used as the reference velocity. The aspect ratio of the flow was 5:1 and, as a result, was found to become immediately 3D via an interaction of the starting vortex with the lateral walls within the channel. Some comparisons to the work of Huang and Fiedler (1997) were made and are discussed in that paper.

Scarano and Riethmuller (1999) performed PIV measurements on a BFS flow at a step height Reynolds number of $Re_h\approx$5,000. Two recirculation bubbles were identified from the mean velocity field (a primary and a corner eddy) with a mean reattachment length of 5.9h. Statistical quantities, $\overline{u'^2}$, $\overline{v'^2}$ and $\overline{u'v'}$, were calculated from the sampled velocity fields. Comparisons with the direct numerical simulation data of Le et al. (1997) were in reasonable agreement, both qualitatively and quantitatively, with differences not exceeding 20% of full scale values. They attributed this scatter primarily to the low number of samples considered, i.e. 208. A further analysis of this data by Scarano et al. (1999) utilised a pattern recognition technique in an effort to characterise the spatial occurrence and size of spanwise vortices in and around the shear layer. A larger occurrence of counter-clockwise structures was found in the step corner than in the free shear layer. They suggested that the clockwise vortices arose from a Kelvin–Helmholtz instability in the shear layer, while the counter-clockwise vortices were due to a 3D breakdown of the clockwise vortices. The formation, roll-up and shedding of spanwise vortical structures in the separated shear layer was also identified using the out of plane vorticity component, ω_z, and topological flow visualisation concepts based upon the velocity gradient tensor in a plane. However, the latter technique possesses some coherent structure identification problems, as outlined by Perry and Chong (1994), since it is impossible to unambiguously identify 3D topology from two-component, 2D data only. Turbulent kinetic energy production in the flow was found to peak early in the shear layer, at $x/h\sim1.6$ and

$y/h \sim 1$, where the roll- up of the primary vortices in the shear layer was most likely to be occurring.

The principal aim of the present investigation was to conduct a detailed experimental study, using PIV, of the structure and behaviour of a separating and reattaching turbulent boundary layer over a BFS. Two-dimensional (2D), spatio-temporal, measurements of velocity and vorticity within and around a closed separation bubble in the x–y and x–z planes were made. Flow visualisation images are also presented to support the PIV data. The in-plane Reynolds stress and turbulent kinetic energy production distributions were also measured. These measurements were used to study the flow physics and structure of flow separation and reattachment using the concept of coherent structures, which are identified from the measured velocity and vorticity fields.

The technique of proper orthogonal decomposition (POD) is used to identify coherent structures in the flow by performing a decomposition on the measured velocity and vorticity fields. The role of large-scale structures in the flow has also been investigated by isolating their effect on the flow using the most energetic POD modes.

2
POD background theory

The data obtained from PIV measurements is well suited to POD analysis. Current experimental PIV techniques are capable of acquiring several hundred instantaneous planar, two component velocity fields on which 1D or 2D POD may be applied. The aim is to capture most of the kinetic energy of the flow in the least number of modes possible. The snapshot POD technique, first proposed by Sirovich (1987), is performed on both the fluctuating velocity and vorticity fields of a BFS flow measured using digital PIV.

2.1
The direct method

Let $f(x,t)$ be a random vector function on a finite spatial domain D and a finite time interval $0 \le t \le T$. Proper orthogonal decomposition involves solving the following Fredholm-type integral equation

$$\int_D R(\mathbf{x},\mathbf{x}')\psi(\mathbf{x}')\mathrm{d}\mathbf{x}' = \lambda\psi(\mathbf{x}) \tag{1}$$

with $R(\mathbf{x},\mathbf{x}')$ known as the kernel. $R(\mathbf{x},\mathbf{x}')$ is the two-point, averaged spatial correlation function ($\equiv \langle f(x,t)f(x',t)\rangle$) with $\langle . \rangle$ denoting the expected value (or ensemble average). Solution of Eq. (1) gives $\psi^{(k)}(x)$ and λ_k which are the empirical eigenfunctions and eigenvalues respectively. The orthogonality condition implies that eigenfunctions of different order do not interact with each other in which case their scalar product,

$$(\psi^{(k)},\ \psi^{(l)}) \equiv \int_D \psi^{(k)}(\mathbf{x})\psi *^{(k)}(\mathbf{x})\,\mathrm{d}\mathbf{x} = \delta_{\mathrm{kl}} \tag{2}$$

is zero (* represents the complex conjugate). The original data may then be reproduced from a linear combination of the eigenfunctions using Eq. (4) with the time-dependent coefficients, $a^{(k)}(t)$ obtained from the projection of a sample dataset onto the eigenfunction space, i.e.

$$a^{(k)}(t) = \frac{\left(f(\mathbf{x},t),\ \psi^{(k)}(\mathbf{x})\right)}{\left(\psi^{(k)}(\mathbf{x}),\ \psi^{(k)}(\mathbf{x})\right)} \tag{3}$$

The original data set can be reconstructed using

$$f(\mathbf{x},t) \approx \sum_{k=1}^{K} a^{(k)}(t)\psi^{(k)}(\mathbf{x}), \tag{4}$$

which is known as the proper orthogonal decomposition of $f(x,t)$.

2.2
The method of snapshots

In practical situations, the data $f(x,t)$ are limited to a finite number of frames or *snapshots*, M. It can be shown that the matrix equation

$$C\Phi^{(k)} = \lambda_k\Phi^{(k)}, \tag{5}$$

gives equivalent solutions to Eq. (1), (Sirovich 1987). Here C is the spatial correlation matrix

$$C_{m,n} = \tfrac{1}{M}\textstyle\int_D f(\mathbf{x},t_m)f(\mathbf{x},t_n)\mathrm{d}\mathbf{x}, \quad m,\ n = 1,\ \ldots,\ M \tag{6}$$

with $\Phi^{(k)}$ and λ_k being the eigenvectors and eigenvalues of C for the kth mode respectively. The empirical eigenfunctions $\psi^{(k)}(x)$ are constructed from a linear combination of the snapshots using

$$\psi^{(k)}(\mathbf{x}) = \sum_{n=1}^{M} \Phi_n^{(k)} f(\mathbf{x},t_n). \tag{7}$$

The problem has now been reduced to solving an $M\times M$ matrix eigenvalue problem instead of an $N\times N$ problem (where N is the number of spatial points in the domain and in most cases $N>>M$). This technique was first suggested by Sirovich (1987) and is commonly known as the *method of snapshots* or *method of strobes*. The direct method is computationally expensive for high-resolution data on a large spatial domain, while the snapshot method only becomes computationally expensive for large ensemble sizes.

2.3
POD mode energy

The *energy* (spatial mean square value) of an instantaneous flow field variable, $f(x,t_n)$, is represented by

$$E_{\mathrm{tot}} = (f,f) = \int_D f(\mathbf{x},t_n)f(\mathbf{x},t_n)\,\mathrm{d}\mathbf{x} \tag{8}$$

The time average of the energy (time–space mean square value) can thus be expressed as

$$\langle E_{\mathrm{tot}}\rangle = \int_D \overline{f(\mathbf{x})^2}\mathrm{d}\mathbf{x} + \left\langle \int_D f'(\mathbf{x},t_n)^2\mathrm{d}\mathbf{x}\right\rangle = \langle E_{\mathrm{mean}}\rangle + \langle E_{\mathrm{fluc}}\rangle \tag{9}$$

which can be decomposed into a mean and fluctuating component. Note that the expected value operator $\langle . \rangle$ is interchangeable with the integral, since the expected value operator is with respect to time. It can be shown (Holmes 1996) that the energy fraction associated with the kth mode, or eigenfunction $\psi^{(k)}(x)$ is

$$E_k = \frac{\lambda_k}{\sum_{k=1}^{M} \lambda_k}. \quad (10)$$

Using the definition of the inner product given by Eq. (2), the energy of the flow based on the velocity, **u** and the vorticity ω yields the following results

$$\text{kinetic energy density} = \frac{1}{2}\rho(\mathbf{u},\mathbf{u}) = \frac{1}{2}\rho||\mathbf{u}||^2 \quad (11)$$

$$\text{enstrophy density} = (\omega,\omega) = ||\omega||^2 \quad (12)$$

where ρ is the fluid density. Hence, applying POD to **u** and ω will categorise structures according to their contribution of kinetic energy and enstrophy to the flow. Note that these are always positive definite quantities.

3 Experimental facility and flow diagnostics

3.1 Water tunnel

The experimental investigations were conducted in the water tunnel shown in Fig. 2. This is a closed circuit, horizontal facility with five 1-m-long working sections, each of 500 mm×500 mm cross-section. Flow uniformity is achieved with a series of stainless steel screens and a honeycomb in the settling chamber. A perforated plate is placed immediately after the spray system (essentially a large perforated pipe that uniformly distributes water from the pump to the rear of the settling chamber) followed by four screens of decreasing mesh size in the flow direction. The honeycomb section is inserted between the first and second screens to straighten the flow and remove any mean swirl. A 10:1 contraction is used prior to the first working section to further reduce the turbulence intensity by accelerating the mean flow. A maximum flow-speed of 775 mm/s is achievable in the working sections with the current 53 kW a.c. motor and in-line centrifugal pump system.

Control of the motor-pump system speed is achieved with an ABB Sami GS frequency controller which allows incremental steps in tunnel speed of 0.2 mm/s over the entire flow-speed range. A plenum chamber attached to the final working section diffuses the flow and returns it via a 300-mm-diameter pipe to the pump. Perforated stainless steel plates in the plenum chamber, placed vertically and parallel to the working section walls, ensure minimal disturbance to the upstream working section flow while effectively redirecting the flow through 180° into the return pipe. A diatomaceous earth pool filter system running in parallel with the main return flow pipework removes contaminants from the water. The filtration can be activated at any time, but it is not operated during experiments. Further characteristics of the tunnel facility are given in Kostas (2002).

3.2 The BFS flow

The flow geometry used for the BFS experiments is shown in Fig. 1. A plate of thickness h=8 mm constitutes the BFS. This results in an aspect ratio (step span/step height) and expansion ratio (y_2/y_1) of 62 and 1.02 respectively. The plate is positioned 131 mm above the tunnel floor ensuring that the turbulent boundary layer flow is independent of the tunnel floor boundary layer. The mean freestream velocity for the experiments presented in this study is U_∞=425 mm/s, yielding a Reynolds number based on a step height of Re_h=4,660. A 5:1 semi-ellipse is glued on the leading edge of the BFS plate to minimise large-scale separation.

Given the relatively low Reynolds number of the boundary layer in the experiment (Re_θ<6,000; see Erm and Joubert 1991), a trip device is used to facilitate its transition to the turbulent state. The boundary layer is tripped using a roughness element that is placed 117 mm downstream from the leading edge and consists of small acrylic blocks 16 mm long×5 mm wide×6 mm high glued onto a 2-mm-thick polycarbonate strip at 14-mm spanwise intervals. The distance from the boundary layer trip to the trailing edge of the plate is 1,850 mm (≈450θ). The results of Erm and Joubert (1991) show that mean-flow profiles, broadband-turbulence profiles and spectra are found to be affected very little by the type of trip device used (wire, distributed grit, pins) for Re_θ≈1,000 and above, indicating an absence of dependence on flow history for this Re_θ range.

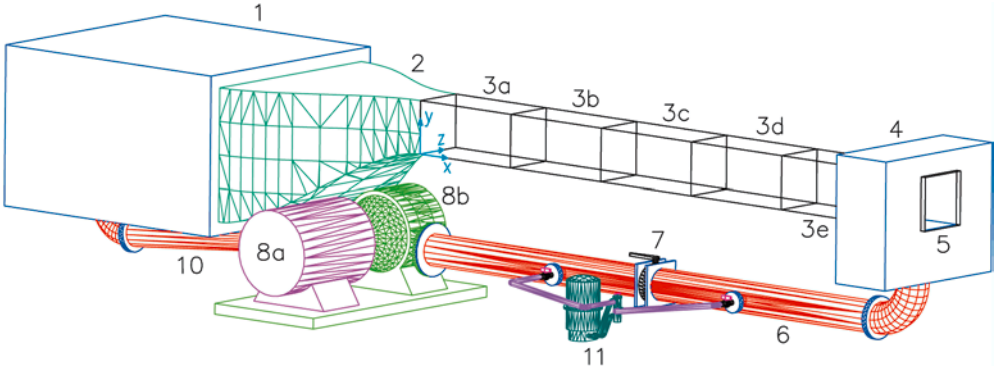

Fig. 2. Closed-circuit horizontal water tunnel used in the experiments. The measurements were taken in working section 3c: *1*, settling chamber; *2*, 10:1 contraction; *3*, working sections; *4*, plenum chamber; *5*, rear observation window; *6*, return pipework – suction side; *7*, filtration isolating valve; *8*, a.c. motor – centrifugal pump system; *10*, return pipework – pressure side; *11*, water filtration circuit

The boundary layer properties prior to separation (18 mm or 2.25h upstream from the trailing edge of the plate) are listed in Table1. These were obtained from the average of 128 instantaneous velocity profiles using cross-correlation digital PIV. The wall shear velocity, u_τ, was obtained using the method of Clauser (1956). u_τ/U_∞ may be obtained directly by plotting the mean velocity profile on coordinates U/U_∞ vs $(U_\infty y/\nu)$ and least squares fitting Eq. (13) to the portion of data exhibiting a clear semi-logarithmic relationship. Figure 3 shows the mean turbulent boundary layer velocity profile plotted in wall coordinates. A universal boundary layer profile is also included in each case for comparison. The universal constant values κ=0.41 and A=5.0 were used for this purpose.

$$\frac{U}{U_\infty} = \frac{u_\tau}{\kappa U_\infty}\ln\left(\frac{U_\infty y}{\nu}\right) + \frac{u_\tau}{\kappa U_\infty}\ln\left(\frac{u_\tau}{U_\infty}\right) + \frac{u_\tau}{U_\infty}A \qquad (13)$$

The spatial resolution of the measurements is insufficient to obtain any data in the buffer ($5<y^+<20$) or linear regions ($y^+<5$). A deviation in the experimental data from the universal profile is present for $y^+<100$ and is most likely due to a bias introduced by a lack of spatial resolution (i.e. measurement volume too large) from the PIV close to the wall. The spatial averaging that occurs as a result of the finite interrogation window size is particularly severe in locations with large gradients (i.e. close to the wall) and in this case results in an overestimation of the particle displacements.

4
Measurement and analysis technique

Cross-correlation PIV of single exposed digital images has been used to acquire instantaneous, in-plane velocity field measurements of the BFS flow. A PCO Sensicam camera (1,280 pixel×1,024 pixel CCD array size) coupled to a Pentium-based PC, with image acquisition and timing software, is used to acquire pairs of singly exposed images. A 105-mm Micro Nikkor lens is used for imaging and provides a field of view of approximately 50 mm×40 mm.

The flow is seeded with 11-μm hollow glass spheres (specific gravity≈1.1) and the flow plane of interest is illuminated with twin, frequency doubled New Wave Research Gemini PIV 15 Nd:YAG lasers. Each laser is capable of producing 4-ns, 125-mJ pulses at a repetition frequency of 15 Hz. An appropriate combination of cylindrical lenses produces a 150-mm-wide by 2-mm-thick collimated light sheet on entry to the test section that illuminates the 2D plane of the flow. Operating the camera lens at f5.6 to f8 results in a depth of field of between 0.1 mm and 0.2 mm (see Adrian 1991), effectively meaning that the velocity measurements are confined to a very thin slice of flow within the light sheet.

The number of images capable of being acquired is dependent on the available PC RAM and the size of the frame acquired. This is limited to 114 full-size (12-bit) image pairs at a framing rate of 4 Hz. Direct acquisition to hard disk permits a larger number of frames to be acquired albeit at a reduced framing rate. This allows the measurement of second-order statistics of flow quantities with a smaller uncertainty. Synchronisation of the lasers and digital camera is achieved by sending TTL signals to the appropriate devices using the PC's parallel port. The timing accuracy of this technique is of the order of 10 μs.

Measurements are taken at multiple x–y planes by traversing the light sheet and camera across the desired regions, shown in Fig. 4. Images in the x–y plane are captured along the centreline of the tunnel, i.e. z=250 mm. Data in the x–z plane are acquired at a number of spanwise planes. The light sheet is adjusted to illuminate x–z regions at $y=h$, $y=0.5h$ and $y=1.5h$. 1,024 image pairs are acquired in the x–y plane in regions I and II, and 114 image pairs are acquired for each of the x–z planes. The time between image pair acquisitions is set to 1 s to ensure that consecutive velocity fields are statistically independent.

Table 1. Boundary layer properties 18 mm (≡ 2.25h) upstream from the BFS. The turbulence intensity value was measured in the freestream. Water properties were evaluated at 35°C and 100 kPa

δ	δ^*	θ	u_τ	U_∞	u_{rms}/U_∞	Re_δ	Re_{δ^*}	Re_θ
42 mm	6 mm	4 mm	19 mm/s	425 mm/s	1.0%	24,490	3,500	2,330

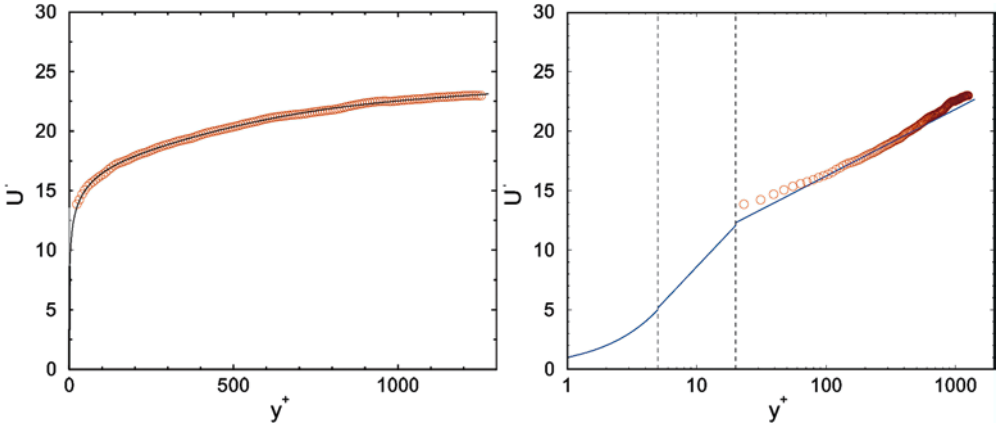

Fig. 3. Boundary layer velocity profile 2.25h upstream from the step edge for Re_h=4,660 (Re_θ=2332): *open circles* represents experimental data. Also plotted for comparison is the universal boundary layer profile, $U^+=y^+$ ($y^+<5$), $U^+=5.0y^+-2.9$ ($5<y^+<20$) and $U^+=1/141\ \ln y^+ +5.0$ ($y^+>20$)

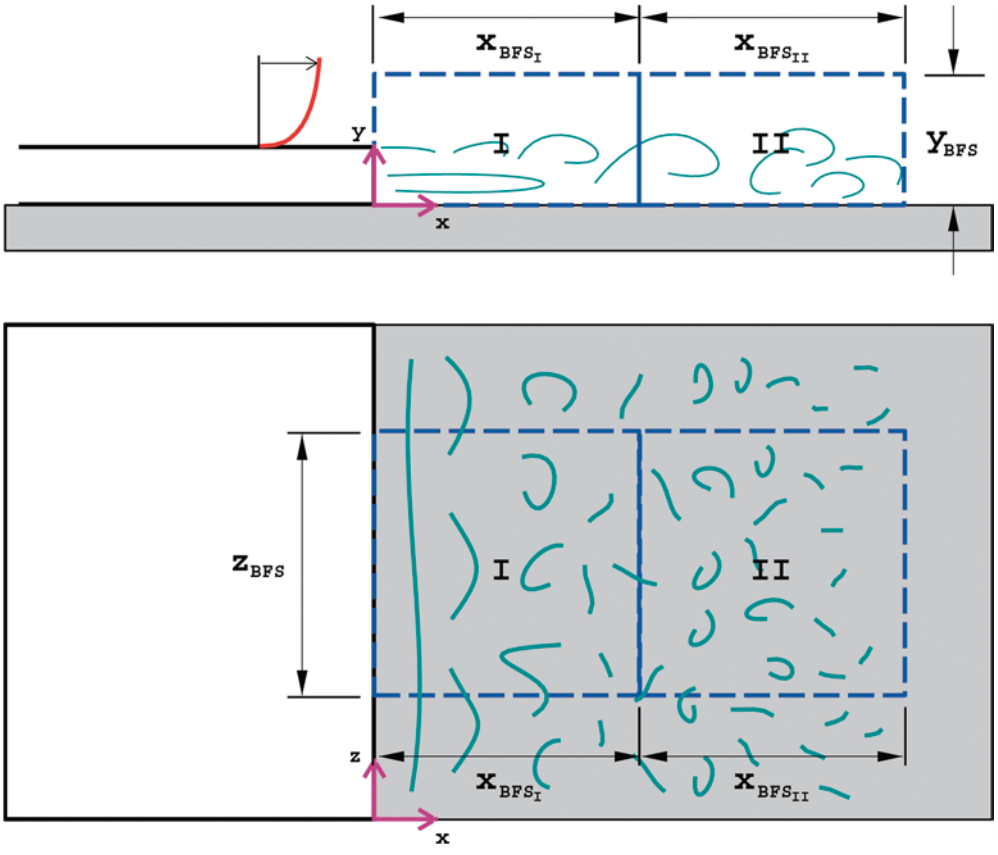

Fig. 4. The PIV measurement regions for the BFS flow: $x_{BFS_I} = x_{BFS_{II}} = 6.25h$; $z_{BFS}=5h$; $y_{BFS}=2.5h$

A multigrid PIV analysis algorithm developed by Soria (1996) and Soria et al. (1999) is used to analyse the images. The technique begins with large sampling window sizes (SWS) and systematically moves to smaller windows by using the displacement estimates from the preceding, larger, window size to offset the small windows. In addition, linear particle image distortion (Huang et al. 1993) is used in regions of the flow where there are high velocity gradients. The use of these techniques permits a large dynamic range of velocities to be resolved in the flow while at the same time preserving spatial resolution by minimising the sampling window size. The minimum resolvable displacement of the multigrid PIV technique used in this investigation is 0.1±0.032 pixels (Soria et al. 1998, 1999).

The PIV analysis of the images acquired in the x–y planes utilised a 32 pixel×32 pixel final SWS (SWS/h=0.16) with a 75% overlap. This resulted in a spatial resolution of 0.16h between independent measurements. Analysis of the images in the x–z planes utilised a 48 pixel×48 pixel final SWS (SWS/h=0.24) with 75% overlap and resulted in a spatial resolution of 0.24h between independent measurements. The maximum in-plane displacement, based on free stream velocity, is 11 pixels. An error of ϵ_u=1.4% (referenced to the freestream velocity) exists in the instantaneous velocity field measurements.

Velocity fields not satisfying a criterion of at least 95% successfully computed vectors are discarded. Rejected vectors are filled using a linear interpolation method based on the surrounding vectors. Vorticity information is calculated using the technique outlined in Fouras and Soria (1998) by performing a local, 13-point, 2D least-squares fit to the velocity field around the point of interest and then calculating spatial gradients from this functional fit. Two errors arise in the calculated out-of-plane vorticity as a result of the χ^2 calculation method. A random error, $\varepsilon_{\omega_{rand}}$, exists due to the error in the velocity field calculation (i.e. the PIV error) and can be considered to have Gaussian-like properties. The other is a bias error, $\varepsilon_{\omega_{bias}}$, which generally results in an underestimation of the peak vorticity value. Both errors depend on the spatial sampling separation of the data, Δ, and on the size of a relevant length scale to be resolved, L, although in an opposing fashion. The length scale used here is the vorticity thickness of the shear layer at separation, $\delta_{\omega_{z_{sep}}} = (U_{max} - U_{min})/\left(\frac{dU}{dy}\right)_{max}$. The errors associated with the instantaneous vorticity measurements are presented in Table 2. Complete details of the vorticity errors and their determination are given in Fouras and Soria (1998). The effect of overlap on vorticity error is discussed in Raffel et al. (1998).

The entire compilation of data consists of two-component, instantaneous velocity flow fields and single-component, instantaneous vorticity flow fields. The (u,v) velocity components are acquired in the x–y plane

Table 2. Vorticity errors arising from the χ^2 calculation method

	ϵ_u	L	Δ/L	λ	$\varepsilon_{\omega_{rand}}$ %	$\varepsilon_{\omega_{bias}}$ %
Re_h=4,660	1.4	$\delta_{\omega_{z_{sep}}}$	0.16	2.8	3.9	−2.1

and the (u,w) components are acquired in the x–z plane. The out-of-plane vorticity is obtained from the velocity field data yielding the ω_z and ω_y components for the x–y and x–z planes respectively.

In addition to the quantitative data available from the PIV measurements, some qualitative information on the flow structure and dynamics is acquired using planar laser induced fluorescence (PLIF). Experiments are performed in both the x–y and x–z planes of the flow and the optical arrangement is identical to that used in the PIV experiments. Sulforhodamine B (Exciton Kiton Red 620) dye is used in all the PLIF experiments. Further details of the technique can be found in Kostas (2002).

Snapshot POD analysis is applied to both the velocity and vorticity data. The presence of two inhomogeneous directions in the BFS flow (streamwise, x, and cross stream, y) means that the techniques, such as shot noise decomposition (Holmes et al. 1996; Herzog 1986; Moin and Moser 1989; Arndt et al. 1997), for dealing with homogeneous directions are not required. The phase information of the expansion coefficients is obtained directly during flow field reconstruction by projecting the original PIV measurements onto the calculated modes using Eq. (3).

5
Results

5.1
The mean flow structure

In this section, mean flow quantities in the x–y and x–z planes are presented. Measurements obtained using PIV include planar, two-component velocity, out-of-plane vorticity, Reynolds stresses and turbulent kinetic energy production. The data presented are an amalgamation of these mean flow statistics for regions I and II. Regions I and II are overlapped by 5 mm ($\equiv 0.64h$) to ensure as few data as possible are lost in the region adjoining the two measurement areas. A third-order polynomial interpolation is used to smoothly match the data at the interface of the two regions.

The mean velocity field in the x–y plane is shown in Fig. 5. Streamlines are also included in the figure to highlight the mean flow structure. A maximum uncertainty of approximately 1% (based on freestream velocity) exists in the mean measurements. A region of recirculating flow is clearly visible in the flow as is a secondary recirculation region at the step corner. The mean reattachment point occurs where the streamline originating at the step edge, i.e. x=0, y=h, impinges onto the surface. A value of $4.8h\pm0.2h$ for the mean reattachment point is obtained. This value cannot be determined with great accuracy as the data do not extend completely to the floor. The relatively short mean reattachment length, when compared with other experimentally determined values, which range from $4.9h$ to $8.2h$ (see review by Eaton and Johnston 1981), is possibly due to the high turbulence levels close to the floor in the upstream boundary layer ($u_{\rm rms}/U_\infty\approx7\%$ for $y^+<100$ and $v_{\rm rms}/U_\infty\approx4\%$ for $y^+<500$). The large size of the boundary layer, with respect to the step, means the separated shear layer is only likely to feel the effect of the boundary layer turbulence and any effect of freestream turbulence will be negligible.

The mean, non-dimensional, out-of-plane vorticity in the x–y plane, $\omega'_z=\omega_z h/U_\infty$, is shown in Fig. 6. Random and bias errors of 6.4% and 2.1% respectively are present in the mean measurements. The shear layer appears as a concentrated region of negative vorticity that detaches from the step edge and grows in width with increasing streamwise distance. Peak values of ω'_z occur in the shear layer at separation and attain a value of $\omega'_z=-3.4$. The vorticity distribution is initially very thin and spreads downstream to a more bulbous shape between x=2h and x=5h. The large degree of mixing in this region is likely to be the cause of this shape. Downstream of the mean reattachment point, the vorticity continues to decrease as the boundary layer begins to redevelop.

There is a clear absence of negative vorticity in the lower left region of the recirculation zone. The negative vorticity is distributed predominantly around the mean separation streamline. A small region of positive vorticity is present in the step corner, representing the secondary recirculation zone.

Contours of mean, non-dimensional vorticity ($\omega'_y=\omega_y h/U_\infty$) at various cross-stream planes are presented in Fig. 7. The spotted or noisy appearance is due to the uncertainty in the measurements arising from the relatively small number of samples which were available to calculate the mean. Random and bias errors of 11.2% and 2.1% respectively are present in the mean measurements. Nevertheless, a strong organisation of vorticity streaks in the streamwise direction is evident in the mean ω'_y distribution at y=h. Any streamwise organisation of vorticity streaks diminishes downstream of the mean reattachment point. There also appears to be little structure in the highest plane y=1.5h, while the plane y=h shows a strong organisation of alternating ω'_y patches centred on $x\approx1.5h$. The plane closest to the floor shows a tendency for ω'_y activity to lie near the reattachment point. A distinct lack of high vorticity concentration is apparent in the region

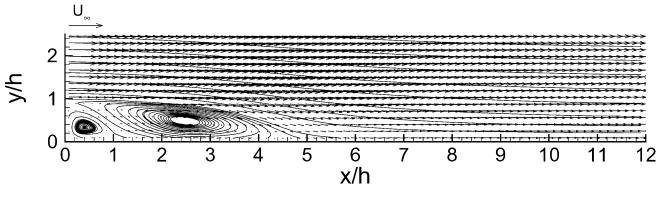

Fig. 5. Mean 2D velocity field and integral curves in the x–y plane (only every fourth vector is shown for clarity). The velocity measurements were normalised by freestream velocity, U_∞

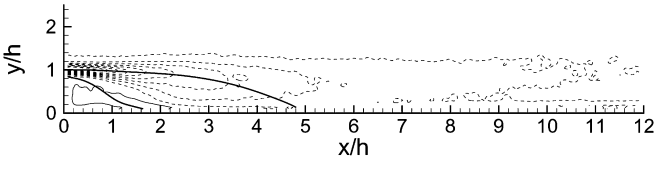

Fig. 6. Non-dimensional, mean out-of-plane vorticity, $\omega'_z=\omega_z h/U_\infty$, in the x–y plane, contours: –3.0, –2.7, –2.3, –2.0, –1.6, –1.3, –0.9, –0.6, –0.2, 0.1 The mean primary and secondary separation streamlines are also shown

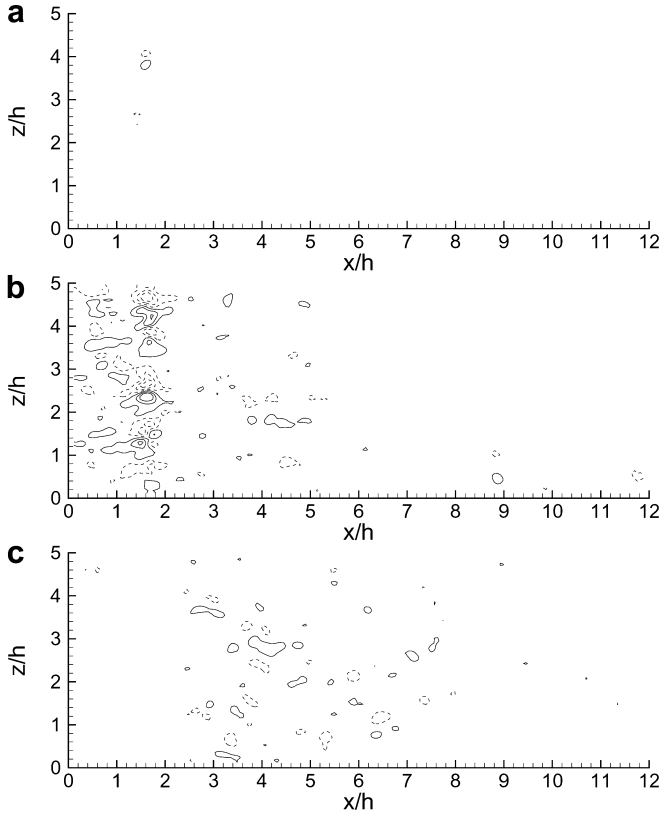

Fig. 7a–c. Non-dimensional, mean out-of-plane vorticity, $\omega'_y=\omega_y h/U_\infty$, at the x–z planes: **a** y=1.5h; **b** y=h; **c** y=0.5h; contours: –0.7, –0.42, –0.14, 0.14, 0.42, 0.7

close to the step for the y=0.5h plane, suggesting relatively little intense ω'_y activity close to the step corner. This behaviour is also observed for the ω'_z component.

A spanwise autocorrelation of ω'_y in Fig. 7b is presented in Fig. 8. Also included in the plot is the spanwise autocorrelation of ω'_y vorticity streaks of a 40 mm×50 mm portion of the boundary layer just prior to the step (at a plane 4 mm above the step). The non-dimensional streak spacing obtained from the plot is $200 \lesssim \lambda^+ \gtrsim 300$ ($\equiv h \lesssim \lambda \gtrsim 1.5h$) and falls within the generally accepted range of $50<\lambda^+<300$ for turbulent boundary layers (Smith 1996). This streak spacing closely coincides with the spacing of the trip elements. However, this similarity may be purely coincidental as the results of Erm and Joubert (1991) suggest there is no apparent history of any influence of the trip device in the boundary layer structure approximately 40–50 boundary layer thicknesses downstream distance from the trip for $Re_\theta \approx 2{,}000$.

Results of a DNS of a BFS flow at a Re_h=6,000 by Neto et al. (1993) show a presence of intense, slightly inclined streamwise vortices strained between primary spanwise vortical structures. Longitudinal streaks are also observed in mixing layers (Rogers and Moser 1992; Brown and Roshko 1974) and in separated shear layers (Ruderich and Fernholz 1986). Thus, the observed vorticity streaks in Fig. 7b can be thought of as the natural response of the separated shear layer to upstream boundary layer streaks.

The x–y plane Reynolds stress components $\overline{u'^2}$, $\overline{v'^2}$ and $-\overline{u'v'}$ are shown in Fig. 9a, b and c respectively. An uncertainty of 8.6% (at the 95% confidence level) is present in the measurements. The largest values of Reynolds stress are found before reattachment, with maximum values occurring approximately one plate thickness before reattachment at a cross stream height of $y \approx 0.7h$. A decline in the stresses is observed soon after reattachment for all the x–y plane components. Appreciable values of $\overline{u'^2}$, $\overline{v'^2}$ and $-\overline{u'v'}$ begin to develop two plate thicknesses after separation at a height of $y \approx h$ in a narrow region centred on the shear layer. The shape of the distribution of the three x–y plane Reynolds stress components compares well with the data of Scarano and Riethmuller (1999), Le et al. (1997) and Chandrsuda and Bradshaw (1981) among others. Peak values of the Reynolds stresses are listed in Table 3 and also agree well with previously published data (see review by Eaton and Johnston 1981).

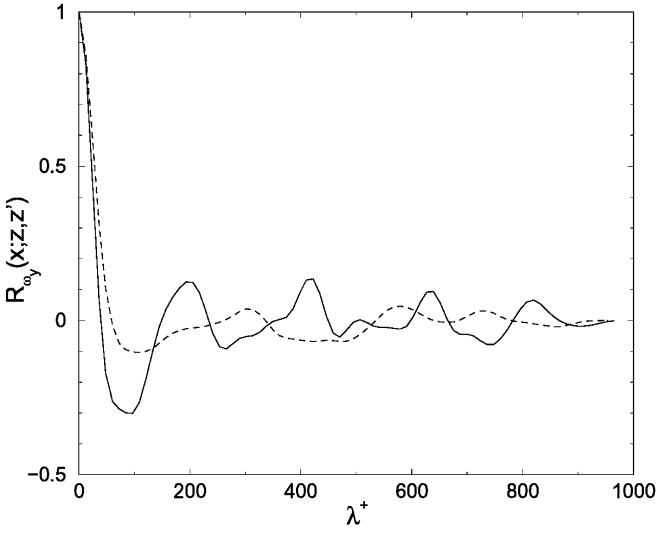

Fig. 8. Spanwise auto-correlation function, $R_{\omega_y}(x;z,z')$, of mean ω_y: *solid line*, $R_{\omega_y}(x;z,z')$ at approximately 2h downstream of separation, y=h, x–z plane; *dashed line*, $R_{\omega_y}(x;z,z')$ of upstream boundary layer, y=1.5h, x–z plane

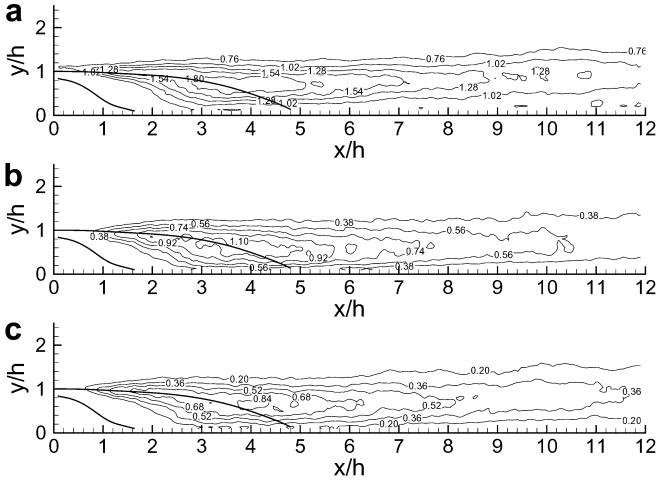

Fig. 9a–c. Reynolds stress distributions in the x–y plane: **a** $\overline{u'^2}/U_\infty^2 \times 100$; **b** $\overline{v'^2}/U_\infty^2 \times 100$; **c** $-\overline{u'v'}/U_\infty^2 \times 100$. The mean primary and secondary separation streamlines are also shown

Table 3. Maximum Reynolds stress values in the flow

$\overline{u'^2}/U_\infty^2$	$\overline{v'^2}/U_\infty^2$	$w'^2/\overline{U_\infty^2}$	$\overline{-u'v'}/U_\infty^2$	$-\overline{u'w'}/U_\infty^2$
2.12×10^{-2}	1.29×10^{-2}	2.11×10^{-2}	0.94×10^{-2}	0.55×10^{-2}

The turbulent kinetic energy production in the flow is illustrated in Fig. 10. An uncertainty of 19% (at the 95% confidence level) is present in the measurements. The location of the peak turbulent kinetic energy production occurs further upstream than the location of the peak in any of the Reynolds stress distributions. This is attributed to the dependence of the turbulent kinetic energy production on both the Reynolds stress components and the mean spatial velocity gradients. Large velocity gradients occurring close to the BFS tend to bias the turbulent kinetic energy production upstream of the peaks in the Reynolds stresses.

The turbulent kinetic energy production distribution agrees with the previously published results of Le et al. (1997) and Scarano et al. (1999) and attains a peak value of $P_{\mathrm{ke}}^{2D} = \left[\overline{u'^2}\frac{\partial U}{\partial x} + \overline{v'^2}\frac{\partial V}{\partial y} + \overline{u'v'}\left(\frac{\partial U}{\partial y} + \frac{\partial V}{\partial x}\right)\right] \Big/ \left(h/U_\infty^3\right) = 1.2\times10^{-2}$ in the early portion of the separated shear layer.

The bulk of the turbulent kinetic energy production occurs in a region situated along the mean separation streamline. Maximum production is localised in a thin strip within the shear layer at $y\approx h$ that extends from $x\approx h$ to $x\approx 2h$. This marks the location of strong longitudinal shear, $\partial U/\partial y$, and relatively intense Reynolds shear stress, $-\overline{u'v'}$. Beyond this region, the turbulent kinetic energy production decreases to a uniform value of approximately $P^{2D}{}_{\mathrm{ke}}\approx 0.6\times10^{-2}$ and adopts a distribution of similar shape and spatial extent to the Reynolds shear stress distribution.

5.2 The instantaneous flow structure

This section presents the instantaneous vorticity fields and flow visualisation images in the x–y planes to illustrate the instantaneous structure of the BFS flow. One of the key features of separated flows is the presence of isolated, spanwise vortical structures in the shear layer. According to the definition suggested by Robinson (1991), vortices appear as concentrated regions of vorticity around which the pattern of streamlines is focal in nature in a frame of reference moving with the centre of the vortex. These structures play a key role in the dynamics of the flow and are largely responsible for the shear layer growth and momentum transfer across the shear layer. They originate from a Kelvin–Helmholtz type instability in the shear layer, which leads to the growth of waves that eventually roll up into discrete vortical structures. The vortex structures subsequently convect downstream and grow in size via pairing interactions as observed in plane mixing layers (Winant and Browand 1974).

Vortices are regularly observed in the flow and can be seen in the instantaneous PIV data presented in Fig. 11. Multiple structures are not always observed in an in-line configuration as shown in Fig. 11a but also sometimes in a staggered formation, as in Fig. 11b. The array of vortices often persists all the way to the reattachment point and suggests different modes of shedding may be present in the flow. The small size and close spacing of the vortical structures means that there is likely to be a number of vortical interactions occurring before reattachment.

Fewer discrete structures are identifiable from the flow visualisation images than from the instantaneous vorticity fields. However the first few structures in the shear layer still exhibit the classic Kelvin–Helmholtz roll-up. This is apparent in the flow visualisation images of Fig. 12a and b. The flow visualisation data does not show evidence of the staggered vortex train observed in the PIV data, as the dye diffuses far too quickly to be able to make any discrete vortical structures after two to three step heights.

Although vortices and vortex interactions have been identified from flow visualisation images of separated flows (Soria et al. 1993; Cherry et al. 1984; Roos and Kegelmann 1986), there has been little evidence of their detection from PIV measurements. This type of quantitative observation would give further support to the idea that the mixing layer and separated shear layer have similar growth mechanisms.

Vortex pairing events were captured in the PIV, and flow visualisation data of both flows and are shown in Figs. 13 and 14. The pairing sequence captured in Fig. 14

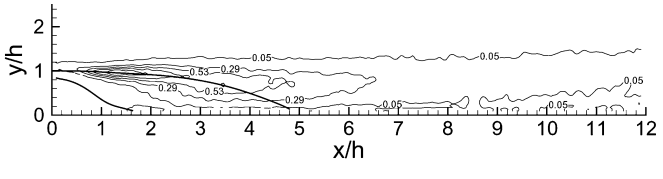

Fig. 10. Normalised turbulent kinetic energy production, $P_{\mathrm{ke}}^{2D} = \left[\overline{u'^2}\frac{\partial U}{\partial x} + \overline{v'^2}\frac{\partial V}{\partial y} + \overline{u'v'}\left(\frac{\partial U}{\partial y} + \frac{\partial V}{\partial x}\right)\right] \Big/ \left(h/U_\infty^3\right) \times 100$. The mean primary and secondary separation streamlines are also shown

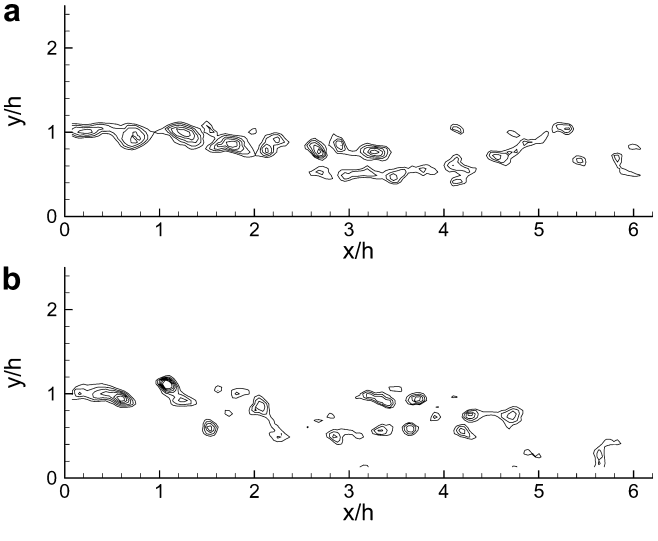

Fig. 11. a, b Instantaneous vorticity fields from region I in the x–y plane illustrating vortical structures in the shear layer. Contours of out-of-plane vorticity are shown, $\omega'_z=\omega_z h/U_\infty$: –5, –4.4, –3.8, –3.2, –2.6, –2

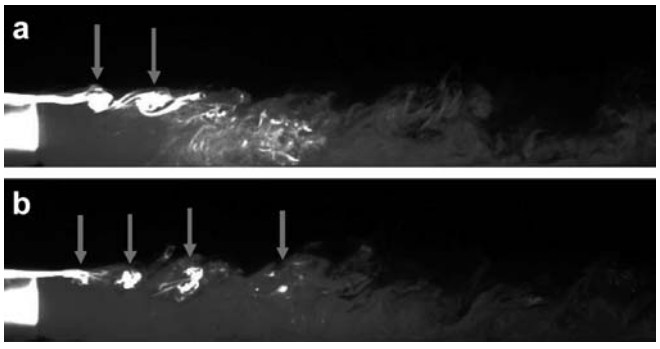

Fig. 12. **a, b** Flow visualisation images showing the presence of discrete vortical structures in the flow. The structures are indicated by *arrows*. The images span 10*h* in the streamwise direction

resembles the flow visualisation pairing sequences captured in a plane mixing layer by Winant and Browand (1974), although it is likely to be a turbulent pairing event, as there is a disordered distribution of dye in the vortical structures.

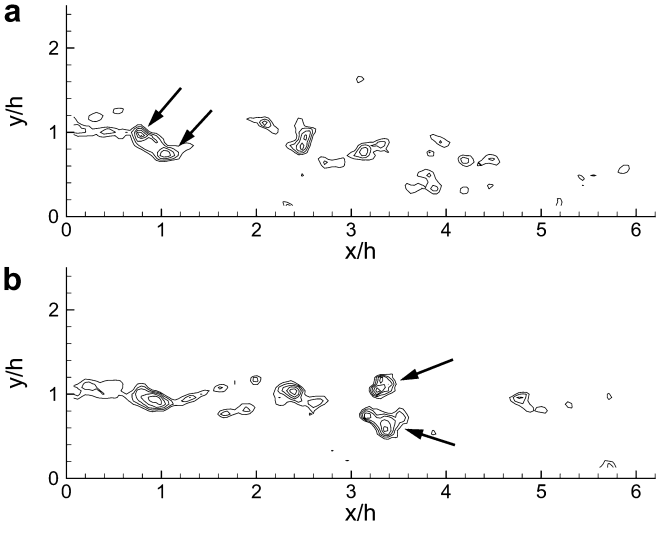

Fig. 13. **a, b** Instantaneous vorticity fields from region I in the *x–y* plane illustrating pairing events in the shear layer. The structures undergoing pairing are indicated by *arrows*. Contours of out-of-plane vorticity are shown, $\omega'_z=\omega_z h/U_\infty$: –5, –4.4, –3.8, –3.2, –2.6, –2

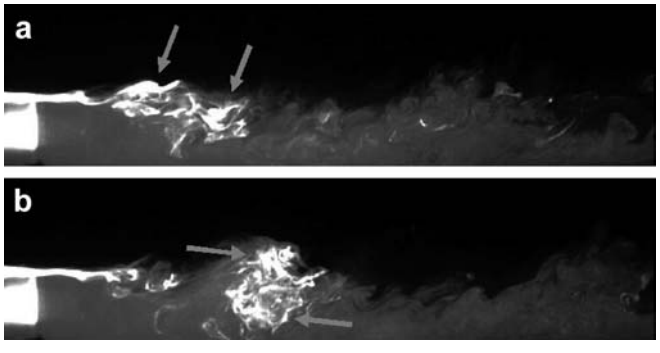

Fig. 14. **a, b** Flow visualisation images showing a turbulent pairing event. The images span 10*h* in the streamwise direction

The shear layer roll-up process (and early pairing events) do not appear to contribute in any significant way to the production of any Reynolds stresses. This is evident from the low levels of Reynolds stress in the region between separation to the first appearance of vortical structures in the flow, i.e. $x \lesssim 2h$ (see Fig. 9). Browand and Weidman (1976) show that vortex pairing events are undoubtedly associated with Reynolds stresses in the flow. This is observed in the current investigation where the more downstream, turbulent interactions coincide with the locations of high Reynolds stress in the flow.

Reynolds stresses are found to remain at levels greater than 60% of peak values for at least one plate thickness after the mean reattachment point. This suggests continuing vortex activity in that region and this can be seen in the instantaneous vorticity fields of Fig. 15, where a number of pairing interactions were captured after reattachment. A large organisation of inclined vortices and vortex packets in the flow are also found after reattachment. Such structures are also observed in the turbulent boundary layer measurements of Adrian et al. (2000b). The relatively large scales of these vortex packets in the redeveloping region of the BFS flow leads to the suggestion that large-scale structures are responsible for the production of turbulent stresses in the region after reattachment.

5.3 POD results

The POD modes represent the most common events occurring in the fluctuating velocity/vorticity fields. Modes 1, 4, 10 and 25 from the vorticity decomposition are shown in Fig. 16. They contribute 1.38%, 1.22%, 0.93% and 0.61% respectively to the total fluctuating enstrophy in the flow. These are very small energy contributions compared with the corresponding velocity modes which contribute 13.11%, 3.36%, 1.62% and 0.61% to the total fluctuating kinetic energy in the flow. This result is suggestive of a

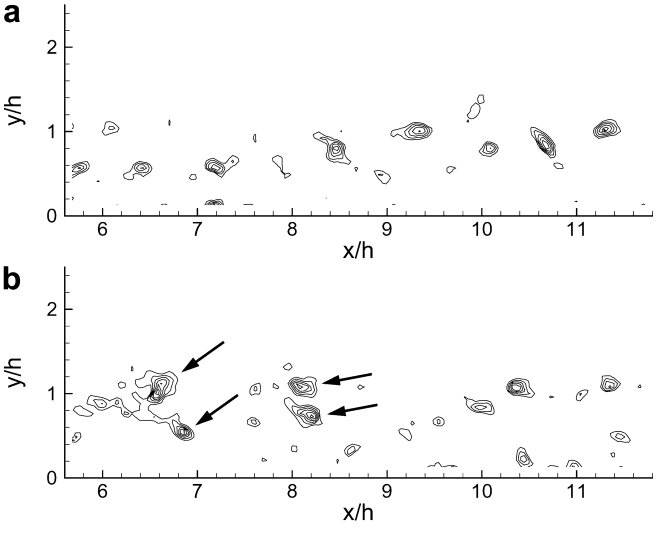

Fig. 15. **a, b** Flow structure and vortex activity in the redeveloping region. The structures undergoing pairing are indicated by *arrows*. Contours of out-of-plane vorticity are shown, $\omega'_z=\omega_z h/U_\infty$: –4.5, –3.9, –3.3, –2.7, –2.1, –1.5

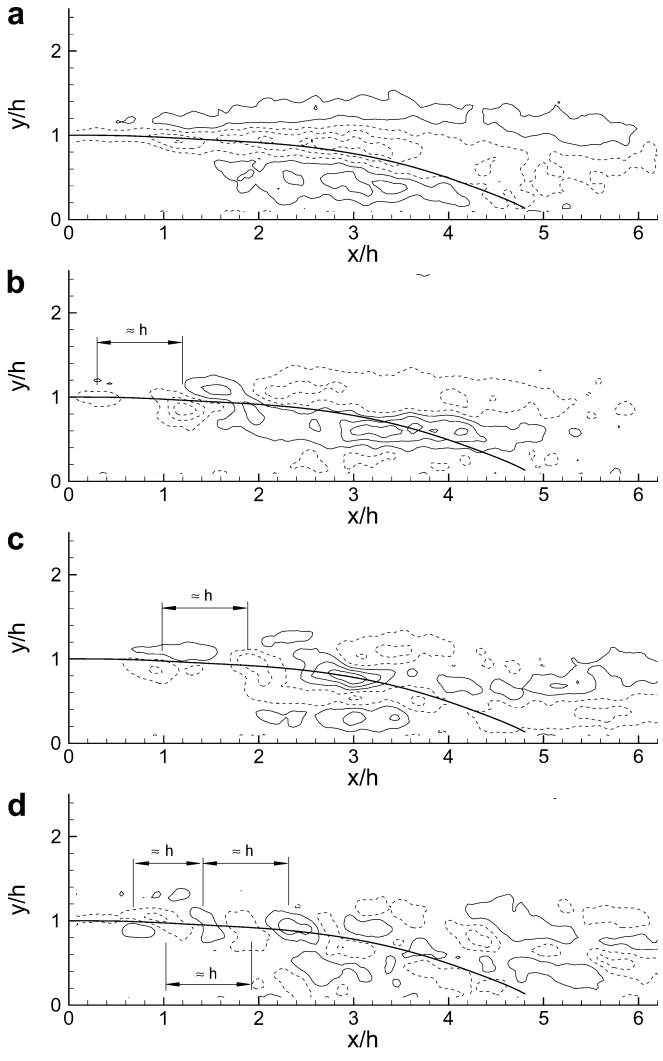

Fig. 16a–d. Vorticity POD modes: **a** 1; **b** 4; **c** 10; **d** 25 in region I. Contours of non-dimensional vorticity are shown, $\omega'_z=\omega_z h/U_\infty$: –0.3, –0.18, –0.06, 0.06, 0.18, 0.3

greater diversity of flow structure in the vorticity field than the velocity field and results in a more even distribution of energy between the modes and hence, a less efficient decomposition.

A comparison between the spatial structure of the velocity and vorticity modes was made by calculating the curl of the velocity modes. With the exception of mode 1, there is no apparent one-to-one correspondence between the structure of the velocity and vorticity modes (i.e. vorticity mode i is distinctly different from the curl of velocity mode i). However, this result may be dependent on the choice of ensemble average subtracted from the data before performing the POD analysis (Graham and Kevrekidis 1996). In the present analysis, the time average or mean flow was subtracted. Generally, though, the vorticity modes tend to highlight vortical structures more clearly than the curl of the velocity modes. It therefore seems more appropriate to utilise vorticity as the variable of choice in a POD analysis for detecting coherent structures in turbulent flows. Furthermore, the POD modes obtained from a vorticity decomposition can be used in determining a basis for constructing simplified vortex skeletons of turbulent flows, as performed by Perry and Chong (1987).

A trend noticeable in the progression towards higher modes is the increase in small-scale structure within them. This can be clearly seen in the comparison between vorticity mode 1 and vorticity mode 25, shown in Fig. 16. The small scales are found to contribute only a small fraction to the total fluctuating energy of the flow. However, they still appear to represent physically meaningful flow structures. The modes comprise a variety of structures but primarily contain inclined vorticity sheets and round and elongated vorticity concentrations.

These elongated vorticity regions appearing in the vorticity modes (and also in the curl of the velocity modes) arise from the averaging nature of the POD procedure on the ensemble of uncorrelated snapshots used in the present analysis. Vortical structures are often found in similar regions of the flow but not always exactly in the same place. The averaging nature of the POD analysis consequently "smears" the vorticity structures over the area in which they most often appear, resulting in an elongated distribution of their vorticity in the modes.

A small degree of elongation in the vorticity concentrations is indicative of a relatively consistent organisation of structures in space. This is found to occur at locations close to the step i.e. $x \lesssim 1.5h$, where significant levels of Reynolds stresses have not yet developed.

A comparison between the instantaneous PIV measurements and the POD modes shows how the location of structures in the POD modes coincide with the location of flow structures in the PIV measurements. This is illustrated in the comparison of the instantaneous vorticity fields shown in Figs. 11 and 13, with the POD vorticity modes presented in Fig. 16. Isolated concentrations of vorticity in the vorticity modes can be seen at a number of locations along or near the mean separation streamline (where the actual vorticity structures are most often found).

The vorticity POD modes 4, 10 and 25 shown in Fig. 16 show the presence of uniformly shaped vortical structures (either positive or negative) within approximately 1.5 plate thicknesses of the step. Their relatively round shape and regular streamwise spacing (approximately half a plate thickness between oppositely signed vorticity regions and approximately one plate thickness between similarly signed vorticity regions) offers evidence for a strong organisation of vortical structures close to the step. Vorticity structures appear to develop almost immediately after separation. This can be seen in vorticity mode 4, where a vorticity concentration is present at $x \approx 0.3h$, $y \approx h$. Additionally, a relatively consistent streamwise spacing of approximately h exists between similarly signed vorticity structures for $x<2h$ in the presented modes. This may be an indication of a preferred streamwise wavelength of the spanwise vortices in the flow.

6 Discussion

Low-order representations of the instantaneous, x–y plane, velocity fields, $u(x,y,t_n)$, were reconstructed with the computed velocity modes, $\psi^{(k)}(x)$, using Eq. (14). Their

corresponding Reynolds stress and turbulent kinetic energy production distributions were calculated and compared with the distributions obtained from the PIV measurements. Using the inhomogeneous spatial filtering property of POD (see Adrian et al. 2000a), one is able to investigate the contribution of the various length scales in the flow to the mean turbulence structure.

$$\mathbf{u}(x, y, t_n) \approx \mathbf{u}(x, y) + \sum_{k=1}^{K} a^{(k)}(t_n)\psi^{(k)}(x, y) \qquad (14)$$

The reconstructions of the mean Reynolds stress distributions using k=5, 10, 25 and 50 modes are illustrated in Figs.17, 18 and 19, respectively. The distribution obtained from the PIV measurements is also included in each figure for comparison. The figures illustrate the cumulative effect of using increasingly more modes in the data reconstruction.

The intermediate, background stress levels (i.e. approximately 50% of the maximum values) are well represented in the reconstructions. Good qualitative and quantitative agreement of the background stress levels is achieved with the measured distributions using approximately 25 modes in the reconstructions. Low-order modes (i.e. large-scale structures) appear to be responsible for the majority of the background stress levels as well as the bulk of the stress distribution beyond reattachment.

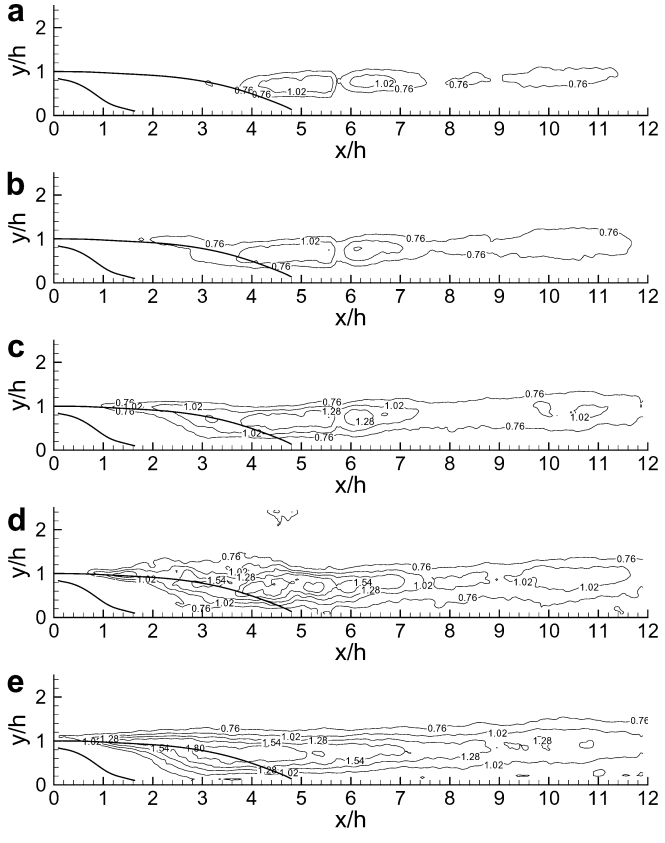

Fig. 17a–e. Normalised Reynolds stress, $\overline{u'^2}/U_\infty^2 \times 100$, obtained using: **a** 5; **b** 10; **c** 25; **d** 50 modes in the reconstruction; and **e** from PIV data. The mean primary and secondary separation streamlines are also shown

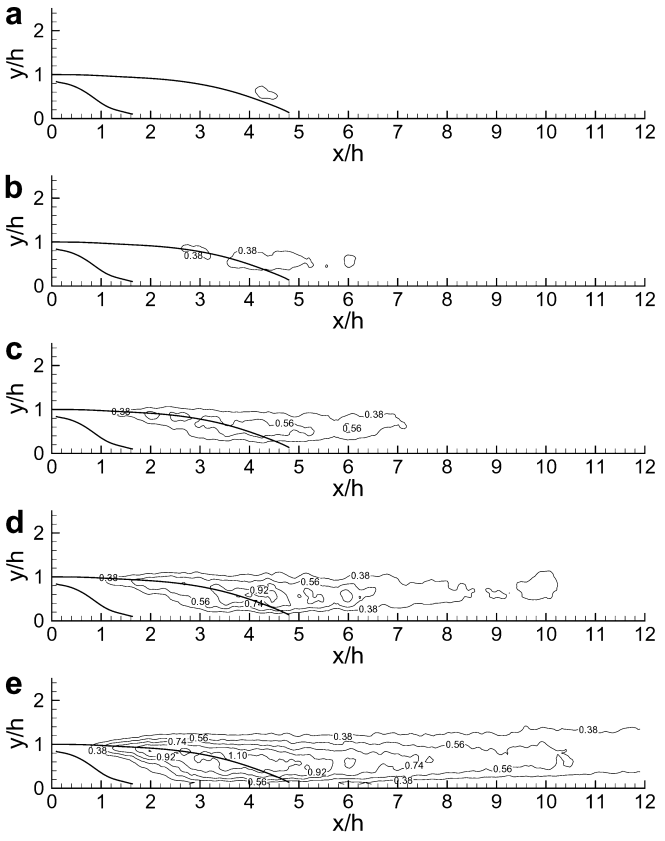

Fig. 18a–e. Normalised Reynolds stress, $\overline{v'^2}/U_\infty^2 \times 100$, obtained using: **a** 5; **b** 10; **c** 25; **d** 50 modes in the reconstruction; and **e** from PIV data. The mean primary and secondary separation streamlines are also shown

The inclusion of higher-order modes (i.e. small-scale structures) contribute to the fine-scale structure and high-intensity stress regions in the reconstructed distributions. For example, the thin, pointed region of stress that is centred upon the mean separation streamline at x<2h and the large, high intensity region centred on x≈4h, y≈0.7h are best represented by the 50 term reconstructions.

An exaggerated stress distribution becomes noticeable in the high Reynolds number flow for the 50 mode reconstruction of the $-\overline{u'v'}$ Reynolds stress component. It seems that once peak stress levels are recovered, the use of increasingly more modes adversely affects the reconstruction. This suggests a poor convergence of the high-order modes in the decomposition which arises from noise in the PIV measurements. A visual inspection of the high-order modes shows that they are noisier than the low-order modes. Details on the effects of ensemble size, data resolution and the presence of random noise in the data on the empirical functions and eigenvalue spectrum calculated using the POD procedure may be found in Breuer and Sirovich (1991).

The $-\overline{u'v'}$ Reynolds stress distribution is the best reconstructed. A recovery of both the peak $-\overline{u'v'}$ stress values and the spatial distribution of $-\overline{u'v'}$ is achieved using approximately 50 modes. A poorer correspondence with the measured distribution is present with the reconstructed distribution of the $\overline{u'^2}$ stress component. At least 50 modes are required before peak stress values are

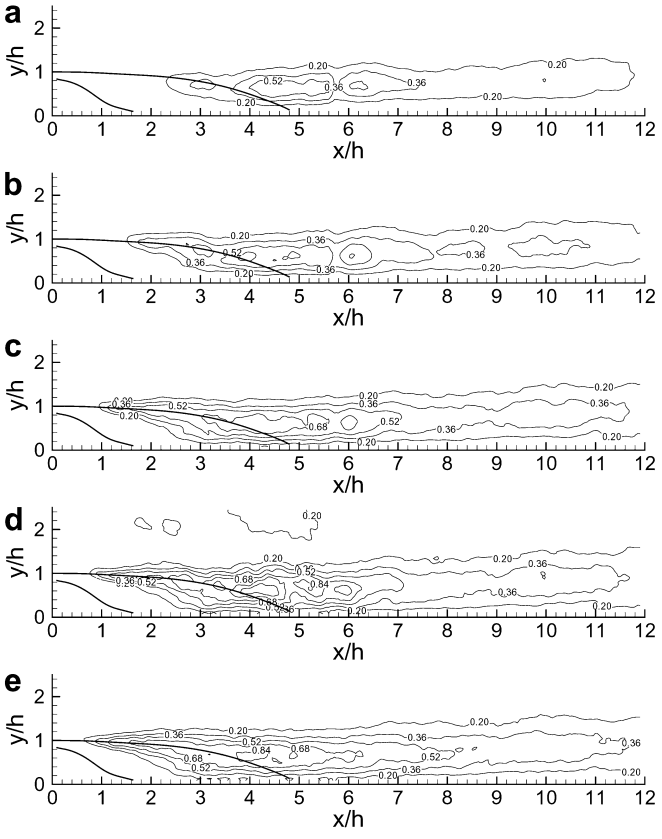

Fig. 19a–e. Normalised Reynolds shear stress, $-\overline{u'v'}/U_\infty^2 \times 100$, obtained using: **a** 5; **b** 10; **c** 25; **d** 50 modes in the reconstruction; and **e** from PIV data. The mean primary and secondary separation streamlines are also shown

recovered and a good qualitative agreement with the measured spatial distribution is obtained. The $\overline{v'^2}$ Reynolds stress component requires in excess of 50 modes to recover the peak stress values. However, the general shape of the reconstructed $\overline{v'^2}$ distribution agrees qualitatively with the measurements.

The contribution of the various length scales to the reconstructed distributions is found to be different for each Reynolds stress component. Large scales contribute very little to $\overline{v'^2}$ stresses. This can be seen in the comparison between the five-term reconstructions of the $\overline{v'^2}$ stress distributions and the five-term reconstructions of the $\overline{u'^2}$ and $-\overline{u'v'}$ stress distributions. Only a small fraction of the background $\overline{v'^2}$ stress levels are recovered, compared with the other two stress components, where a good proportion of the base stress levels is established. Furthermore, the $\overline{v'^2}$ stress component requires more modes in the reconstruction than the other two stress components before peak stress levels and any sense of stress distribution begin to be recovered. This indicates a much greater dependency of $\overline{v'^2}$ on small scales than $\overline{u'^2}$ or $-\overline{u'v'}$.

A comparison between the reconstructed turbulent kinetic energy production using k=5, 10, 25 and 50 modes and the actual measurements is shown in Fig. 20.

Almost 90% of the peak production levels are recovered from the 50 mode reconstruction. The spatial distribution of the reconstructed field also displays a good qualitative agreement with the measurements. The large-scale features, represented by the low-order POD modes, appear to be responsible for the majority of the turbulent kinetic energy production close to reattachment. The high-order modes (small scales) contribute to the intense kinetic energy production that occurs in the thin region along the mean separation streamline between x=h and x=2h.

7 Conclusions

PIV measurements were performed on a BFS flow at a Reynolds number of Re_h=4,660. Regular vortex trains and pairing interactions within the separated shear layer were identified in the instantaneous vorticity measurements. Vortex interactions were found to occur often at the locations where both the turbulent stresses and the turbulent kinetic energy production peak. However, the Reynolds stress maxima occurred further downstream from the turbulent kinetic energy production maxima.

The region of highest turbulent kinetic energy production coincides with the more orderly type vortex interactions where small vortices are likely to undergo a first pairing. The peaks in the Reynolds stresses are most likely to be associated with subsequent vortex parings, vortex growth and transition of the vortices to the turbulent state

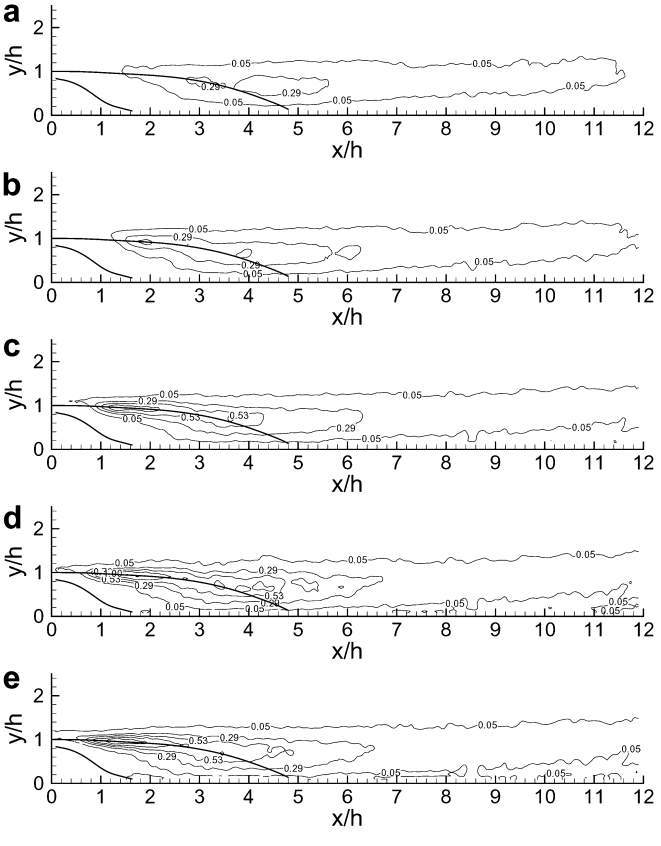

Fig. 20a–e. Normalised turbulent kinetic energy production, $P_{\mathrm{ke}}^{2D} = \left[\overline{u'^2}\frac{\partial U}{\partial x} + \overline{v'^2}\frac{\partial V}{\partial y} + \overline{u'v'}\left(\frac{\partial U}{\partial y} + \frac{\partial V}{\partial x}\right)\right] \Big/ \left(h/U_\infty^3\right) \times 100$, obtained using: **a** 5; **b** 10; **c** 25; **d** 50 modes in the reconstruction; and **e** from PIV data. The mean primary and secondary separation streamlines are also shown

resulting in enhanced mixing over the more planar-like interactions occurring close to the step. The sharp rise in the $\overline{\omega'^2}$ distribution at y=0.4h highlights the region where turbulent vortex interactions occur most often.

Beyond reattachment, the instantaneous PIV data show the presence of relatively large-scale hairpin-like structures, as well as continuing vortex interactions. Similar hairpin structures were observed in the turbulent boundary layer of Adrian et al. (2000b) and more appropriately, the separated turbulent boundary layer of Chong et al. (1998). These structures are responsible for (in addition to the vortex interactions) the persistence of turbulent stresses in the redeveloping boundary layer region.

A proper orthogonal decomposition of the vorticity data reveals the presence of vortical structures throughout the shear layer. Vorticity structures in the modes are found to be most uniform in shape close to the step but become increasingly irregular with downstream distance, suggesting turbulent interactions are occurring at the more downstream locations.

Low-order representations of the mean turbulence quantities suggest that small-scale, orderly vortex interactions are responsible for the most intense turbulent kinetic energy production in the flow. Reynolds stresses are found to peak further downstream from the peak in turbulent kinetic energy production and occur at locations where 3D vortex interactions are most intense. The large-scale structures seem to be largely responsible for the persistence of $\overline{u'^2}$ and $\overline{u'v'}$ in the flow downstream of reattachment, while the $\overline{v'^2}$ stress distribution is governed predominantly by the fine scale structures.

References

Adrian R (1991) Particle imaging techniques for experimental fluid mechanics. Annu Rev Fluid Mech 23:261–304

Adrian R, Christensen K, Liu Z-C (2000a) Analysis and interpretation of instantaneous turbulent velocity fields. Exp Fluids 29:275–290

Adrian R, Meinhart C, Tomkins C (2000b) Vortex organization in the outer region of the turbulent boundary layer. J Fluid Mech 422:1–54

Arndt R, Long D, Glauser M (1997) The proper orthogonal decomposition of pressure fluctuations surrounding a turbulent jet. J Fluid Mech 340:1–33

Breuer K, Sirovich L (1991) The use of the Karhunen–Loève procedure for the calculation of linear eigenfunctions. J Comput Phys 96:277–296

Browand F, Weidman P (1976) Large scales in the developing mixing layer. J Fluid Mech 76:127–144

Brown G, Roshko A (1974) On density effects and large structure in turbulent mixing layers. J Fluid Mech 64:775–816

Brücker C (1999) The 3-D evolution and bursting of the starting vortex downstream of a backward-facing step studied by sequential high-speed scanning PIV. In: Adrian R, Hassan Y, Meinhart C (eds) 3rd International Workshop on PIV. University of California, Santa Barbara

Chandrsuda C, Bradshaw P (1981) Turbulence structure of a reattaching mixing layer. J Fluid Mech 110:171–194

Cherry N, Hillier R, Latour M (1984) Unsteady measurement in a separated and reattaching flow. J Fluid Mech 144:13–46

Chong M, Soria J, Perry A, Chacin J, Cantwell B, Na Y (1998) Turbulence structures of wall-bounded shear flows found using DNS data. J Fluid Mech 357:225–247

Clauser F (1956) The turbulent boundary layer. Adv Appl Mech 4:1–51

deBrederode V, Bradshaw P (1972) Three-dimensional flow in norminally two-dimensional separation bubbles. I: Flow behind a rearward facing step. Technical Report 72-19, Imperial College

Delville J, Ukeiley L, Cordier L, Bonnelt J, Glauser M (1999) Examination of large-scale structures in a turbulent plane mixing layer. Part 1: Proper orthogonal decomposition. J Fluid Mech 391:91–122

Eaton J, Johnston J (1981) A review of research on subsonic turbulent flow reattachment. AIAA J 19:1093–1100

Erm L, Joubert P (1991) Low-Reynolds-number turbulent boundary layers. J Fluid Mech 230:1–44

Fouras A, Soria J (1998) Accuracy of out-of-plane vorticity measurements using in-plane velocity vector field data. Exp Fluids 25:409–430

Gordeyev S, Thomas F (2000) Coherent structure in the turbulent planar jet. Part 1: Extraction of proper orthogonal decomposition eigenmodes and their self-similarity. J Fluid Mech 414:145–194

Graham M, Kevrekidis I (1996) Alternative approaches to the Karhunen–Loève decomposition for model reduction and data analysis. Comput Chem Eng 20:495–506

Grant I, Owens E, Yan Y (1992) Particle image velocimetry measurements of the separated flow behind a rearward facing step. Exp Fluids 12:238–244

Herzog S (1986) The large scale structure in the near wall region of turbulent pipe flow. PhD Thesis, Cornell University

Hilberg D, Lazik W, Fiedler H (1994) The application of classical POD and snapshot POD in a turbulent shear layer with periodic structures. Appl Sci Res 53:283–290

Holmes P, Lumley J, Berkooz G (1996) Turbulence, coherent structures, dynamical systems and symmetry. Cambridge University Press, Cambridge

Huang H (1994) Limitations of and improvements to PIV and is application to a backward facing step flow. PhD Thesis, Technischen Universität Berlin

Huang, H, Fiedler H (1997) A DPIV study of a starting flow downstream of a backward-facing step. Exp Fluids 23:395–404

Huang H, Fiedler H, Wang J (1993) Limitation and improvement of PIV Part II: Particle image distortion, a novel tehcnique. Exp Fluids 15:263–273

Kirby M, Boris J, Sirovich L (1990) An eigenfunction analysis of axisymmetric jet flow. J Comput Phys 90:98–122

Kostas J (2002) An experimental investigation of the structure of a turbulent backward facing step flow. PhD Thesis, Laboratory for Turbulence Research in Aerospace Combustion, Department of Mechanical Engineering, Monash University Melbourne

Le H, Moin P, Kim J (1997) Direct numerical simulation of turbulent flow over a backward facing step. J Fluid Mech 330:349–374

Moin P, Moser R (1989) Characteristic-eddy decomposition of turbulence in a channel. J Fluid Mech 200:471–509

Neto A, Grand D, Métais O, Lesieur M (1993) A numerical investigation of the coherent vortices in turbulence behind a backward-facing step. J Fluid Mech 256:1–25

Perry A, Chong M (1987) A study of eddying motions and flow patterns using critical point concepts. Annu Rev Fluid Mech 19:125–155

Perry A, Chong M (1994) Topology of flow patterns in vortex motions and turbulence. Appl Sci Res 53:357–374

Raffel M, Willert C, Kompenhans J (1998) Particle image velocimetry. A practical guide. Springer, Berlin Heidelberg New York

Rajaee, M, Karlsson S, Sirovich L (1994) Low-dimensional description of free shear flow coherent structures and their dynamical behaviour. J Fluid Mech 258:1–29

Robinson S (1991) Coherent motions in the turbulent boundary layer. Annu Rev Fluid Mech 23:601–639

Rogers M, Moser R (1992) The three-dimensional evolution of a plane mixing layer: the Kelvin–Helmholtz rollup. J Fluid Mech 243:183–226

Roos F, Kegelman J (1986) Control of coherent structures in reattaching laminar and turbulent layers. AIAA J 24:1956–1963

Ruderich R, Fernholz H (1986) An experimental investigation of a turbulent shear flow with separation, reverse flow and reattachment. J Fluid Mech 163:283–322

Scarano F, Riethmuller M (1999) Iterative multigrid approach in PIV image processing with discrete window offset. Exp Fluids 26:513–523

Scarano F, Benocci C, Riethmuller M (1999) Pattern recognition analysis of the turbulent flow past a backward facing step. Phys Fluids 11:3803–3818

Sirovich L (1987) Turbulence and the dynamics of coherent structures. Part 1: Coherent structures. Q Appl Math XLV:561–571
Smith C (1996) Coherent flow structures in smooth-wall turbulent boundary layers: facts, mechanisms and speculation. In: Ashworth PJ, Bennett SJ, Best JL, McLelland SJ (eds) Coherent flow structures in open channels. John Wiley, Chichester, pp 1–39
Soria J (1996) An investigation of the near wake of a circular cylinder using a video-based digital cross correlation particle image velocimetry technique. Exp Therm Fluid Sci 12:221–233
Soria J, Sheridan MJW (1993) Spatial evolution of the separated shear layer from a square leading-edge flat plate. J Wind Eng Ind Aero 49:237–246
Soria J, Kostas J, Fouras A, Cater J (1998) A high spatial resolution and large dynamic range cross-correlation PIV technique for turbulent flow measurements. In: Optical methods and data processing in heat and fluid flow. City University, London, IMechE Conference Transactions, pp 375–384
Soria J, Cater J, Kostas J (1999) High resolution multigrid cross-correlation digital PIV measurements of a turbulent starting jet using half-frame-image-shift film recording. Opt Laser Technol 31:3–12
Winant C, Browand F (1974) Vortex pairing: the mechanism of turbulent mixing-layer growth at moderate Reynolds number. J Fluid Mech 63:237–255